An asymmetric helicase dimer drives 3′-to-5′ DNA unwinding in type II Druantia antiphage defence system

Jun Hou[a,1], Xin Yi[a,1], Wen-Wen Kong[b,1], Yuxin Yang[a], Fengzhi Yuan[a], Peijia Li[a], Hanzhong Feng[a], Zhuangzhuang Chu[a], Long Gui[b *], Yong-Xing He[a *]

[a] Ministry of Education Key Laboratory of Cell Activities and Stress Adaptations, School of Life Sciences, Lanzhou University, Lanzhou, 730000, China.

[b] Institute of Bio-Architecture and Bio-Interactions, Shenzhen Medical Academy of Research and Translation: Shenzhen, 518106, China.

[1]These authors contributed equally to this work.

[*]Correspondence: guilong@smart.org.cn; heyx@lzu.edu.cn.

Keywords: Druantia | Antiviral defence | Helicase | Cryo-EM | Mechanochemical coupling

Abstract

Druantia antiphage defence systems are widespread in bacteria, yet the type II system has remained functionally uncharacterized. Here we show that DruE, the helicase effector of a type II Druantia system from *Pseudomonas protegens* Pf-5, is a 3′-to-5′ helicase that preferentially unwinds substrates bearing a 3′ single-stranded overhang at a duplex junction. Seven cryo-EM structures across the ATPase cycle reveal that DruE forms a constitutive asymmetric homodimer in which two sequence-identical protomers adopt distinct roles. One protomer acts as the translocating motor, threading the 3′ tracking strand through a central channel and coupling nucleotide-dependent conformational

changes to directional movement. The other protomer acts as a clamp, capturing the displaced 5′ strand and gripping the adjacent duplex to potentially prevent strand reannealing. A structural element in the clamp protomer also serves as a strand-separation wedge, a function analogous to the separation pins of canonical helicases but uniquely provided by the non-translocating subunit. These results establish a mechanochemical framework for type II Druantia-mediated immunity and suggest that DruE targets 3′-ended or fork-like phage replication intermediates to suppress infection.

Introduction

Bacteriophages are ubiquitous and continually impose selective pressure on bacteria and archaea, fueling a sustained co-evolutionary arms race[1]. To counter phage predation, prokaryotes deploy a diverse repertoire of antiviral defences. Alongside classic restriction-modification[2] and CRISPR-Cas systems[3], comparative genomic mining has recently revealed a rapidly expanding arsenal of innate mechanisms[4]. These include cyclic-oligonucleotide-based signalling pathways (CBASS)[5], retron-based abortive infection modules[6,7], Gabija[8], and RADAR[9,10], among many others. These systems participate in a wide array of antiphage processes, spanning nucleic-acid surveillance, second-messenger signalling, and programmed cell death (abortive infection)[11], underscoring the extraordinary breadth and dynamics of host–phage interactions.

Helicase-containing antiphage defence systems have emerged as a particularly prominent and mechanistically intriguing class. Superfamily 1 (SF1) and superfamily 2 (SF2) represent the largest groups of helicases, characterized by a conserved ATP-dependent core of RecA-like domains that unwind nucleic acids with strict polarity, while accessory domains diversify substrate recognition and regulation[12]. Recent surveys

indicate that ~20% of non–restriction-modification defence loci encode an SF1/SF2 helicase[13,14] highlighting their frequent repurposing as molecular hubs for sensing and executing antiviral responses. For instance, in the Hachiman system, the Ski2-like DNA helicase HamB continuously surveys intracellular DNA; recognition of exposed 3′ overhangs, which can arise from host-genome damage or phage DNA replication, triggers mechanochemical ratcheting that allosterically activates the HamA nuclease, culminating in indiscriminate DNA degradation and abortive infection[14]. In DISARM, the DrmAB complex is autoinhibited by a trigger loop that is dislodged upon binding to the DNA substrates with a 5′ overhang, initiating long-range activating rearrangements[15,16]. Despite these advances, the mechanistic diversity among immune helicases remains largely underexplored.

Among these defence systems, Druantia is a widespread multi-gene operon recently identified through large-scale genomic mining[9]. Druantia systems encode a large, conserved SF2 helicase, DruE (1800–2100 aa), alongside highly variable, subtype-specific accessory genes. Four major subtypes (I–IV) have been described: type I systems encode four accessory genes (DruA–D), type II encode three (DruM/F/G), type III encode a single accessory gene (DruH), and type IV encode three (DruF/L/K)[17] (Fig. 1a). DruE belongs to the widespread YprA helicase family, characterized by an N-terminal helicase core followed by an oligonucleotide/oligosaccharide-binding (OB) domain, a connector (CON) domain, and a zinc-coordinating DUF1998 domain. Recent comprehensive phylogenomic analyses have identified YprA-family helicases as the central evolutionary "missing link" connecting diverse defence systems, including DISARM and Druantia[18]. However, despite this recognized centrality, how Druantia DruE

helicase engages its DNA substrate and converts ATP hydrolysis into directional unwinding has not been structurally characterized.

Here, we present the biochemical and structural characterization of DruE from the type II Druantia system of Pseudomonas protegens Pf-5. We show that DruE is a DNA-stimulated ATPase and 3′-to-5′ helicase that preferentially engages substrates bearing an exposed 3′ single-stranded end at a duplex junction. Seven cryo-EM structures, including one substrate-free state and six DNA-bound states sampling different nucleotide occupancies, reveal that DruE assembles as a constitutive asymmetric homodimer in which the two protomers adopt distinct functional roles: one acts as the translocating motor along the 3′ tracking strand, while the other captures the 5′ displaced strand and grips the adjacent duplex as a clamp. Structure-guided mutagenesis identifies an Arg1422-associated conformational switch within the motor protomer that couples ATP turnover to directional translocation, and a fork-junction wedge in the clamp protomer that converts translocation into strand separation. Genetic analyses under DNA-damage conditions suggest that the accessory components DruM, DruF, and DruG may restrain DruE activity to limit self-toxicity. Together, these results reveal how two sequence-identical subunits break symmetry to achieve DNA unwinding and offer structural insight into how YprA-family immune helicases may target fork-like replication intermediates during antiphage defence.

Results

DruE, a 3′-to-5′ helicase, is the functional core of the type II Druantia system

While the antiphage activities of Druantia types I and III have been experimentally established[9,19], the type II system (DruMFGE) has remained functionally uncharacterized.

To address this gap, we identified a type II Druantia locus in *Pseudomonas protegens* Pf-5 (Fig. 1a) and heterologously expressed the *druMFGE* operon in *Escherichia coli*. While DruM and DruE were expressed as soluble proteins, DruF and DruG accumulated in the insoluble fraction, hindering reconstitution of the complete type II Druantia system in *E. coli* (Fig. S1). We therefore tested whether the helicase effector DruE alone can mediate phage defence. When challenged with a panel of five bacteriophages (T1, T4, T5, T7, and λ), heterologous expression of DruE produced a detectable but limited protection profile, with the clearest effect against T7 and a weaker effect against T1 (Fig. 1b, Fig. S2). This defence phenotype was strongly reduced by an alanine substitution of Arg1241 within the highly conserved motif VI of the RecA2 domain, a putative "arginine finger" essential for coupling ATP hydrolysis to mechanical transduction. These data indicate that DruE can contribute to antiphage activity in a manner dependent on its catalytic activity (Fig. 1c).

To characterize the enzymatic activity and substrate specificity of DruE, we purified recombinant protein and performed biochemical assays. ATPase assays revealed that DruE possesses DNA-dependent ATPase activity (Fig. 1d). This activity was preferentially stimulated by double-stranded DNA (dsDNA) or structured fork intermediates, whereas single-stranded DNA (ssDNA) or the absence of DNA elicited negligible stimulation, indicating that the ATPase activity of DruE requires duplex or junction-containing DNA. We next performed gel-based helicase assays using DNA substrates with distinct junction topologies (Fig. 1e–h). DruE efficiently unwound substrates harboring a 3′ single-stranded overhang or a Y-fork junction in an ATP-dependent manner (Fig. 1e, f), but was inactive against substrates with 5′ overhangs or

blunt-ended duplexes (Fig. 1g, h). These results establish DruE as a 3′-to-5′ helicase that requires a free 3′ single-stranded tail to initiate duplex unwinding.

To dissect the functional contribution of individual genes within the *druMFGE* locus in the native host, we generated single, in-frame deletion mutants of each gene (Δ*druM*, Δ*druF*, Δ*druG*, and Δ*druE*) in *P. protegens* Pf-5. Under standard growth conditions, all mutant strains exhibited growth kinetics comparable to the wild-type strain (Fig. S3). Intriguingly, upon exposure to MMC, a DNA crosslinking agent that can impede replication fork progression[20,21], deletion of *druE* markedly alleviated MMC-induced toxicity. In contrast, deletion of *druM*, *druF*, or *druG* hypersensitized Pf-5 to MMC (Fig. 1i). Collectively, these findings indicate that DruE contributes to MMC-associated growth inhibition in the native host, whereas DruM, DruF, and DruG are required to maintain fitness under DNA-damaging conditions. This genetic pattern supports a role for the accessory components in limiting DruE-associated toxicity, although the underlying mechanism remains to be defined.

Overall structure of DruE

To elucidate the structural basis of DruE-mediated DNA unwinding, we determined cryo-EM structures of DruE bound to a forked (Y-shaped) DNA substrate, consisting of a 19-bp duplex stem flanked by a 21-nt 3′ and a 6-nt 5′ single-stranded arm, in the presence of Mg^{2+} and either ADP or the non-hydrolyzable analog AMPPNP. Single-particle analysis of the ADP sample resolved a DNA-free apo dimer (3.64 Å) and two substrate-bound DruE–DNA–ADP dimers (3.29 and 3.45 Å), whereas the AMPPNP dataset yielded four substrate-bound dimers in distinct conformations (3.28–3.58 Å) (Figs. S4 and S5; Tables S1 and S2). Local-resolution analyses and representative model-to-map fits for the

AMPPNP and ADP reconstructions are provided in Fig. S6 and Fig. S7, respectively. Collectively, these reconstructions capture DruE in an apo (DNA-free, nucleotide-free) resting state (State I) and six DNA-bound states (States II–VII; Fig. 2a).

Unless otherwise noted, the following architectural description is based on the State VII reconstruction (DruE–DNA–ADP, 3.29 Å resolution), which resolves the most complete set of structural features. In this reconstruction, each DruE protomer comprises a catalytic core of two RecA-like domains, RecA1 and RecA2, which form the ATPase motor. In contrast to canonical SF2 helicases, in which each RecA domain forms a contiguous module, both RecA1 and RecA2 domains of DruE are interrupted by large insertions: RecA1 is split by an anchoring loop (Anc-L), which contacts the DNA duplex and an α-helical insertion (α-Ins), whereas RecA2 is interleaved with a first zinc-binding module (ZBM1), a MarR-like domain, and a second zinc-binding module (ZBM2) (Fig. 2b). Despite this discontinuous primary sequence, the interleaved RecA domains still fold into a single, intact helicase core. C-terminal to the helicase core, DruE comprises a third zinc-binding module (ZBM3), an α-helical domain, an OB-fold tethered to the core through an extended 'Rope' linker, a connector (CON) domain, a DUF1998 domain that also functions as a zinc-binding module (ZBM4), and a terminal iVsr domain[18,22]. Notably, the α-Ins and the α-helical domain are tightly packed around RecA1. In contrast, the MarR-like domain, the zinc-binding insertions, the OB-fold, the CON domain, the DUF1998 module, and the iVsr module are arranged primarily around RecA2, collectively expanding the helicase core (Fig. 2c, d).

In the DruE dimer, the two protomers are related by an approximate two-fold axis, with their MarR-like domains contributing to the primary dimeric interface (Fig. 2d). In the DNA-

bound reconstructions, DruE forms an asymmetric homodimer in which the two protomers differ in both the DNA strand they engage and their nucleotide occupancy, and each protomer forms a central channel that accommodates single-stranded DNA. Notably, the 3′ tracking strand and the 5′ displaced strand enter these two channels through distinct openings on opposite sides of the dimer (Fig. 2e). At the duplex region, only the protomer engaging the 5′ displaced strand contacts the DNA duplex stem through its anchoring loop. Given that DruE is a 3′-to-5′ helicase, the protomer engaging the 3′ tracking strand is likely the translocating motor that drives strand separation, and is therefore referred to as the motor protomer. In contrast, the protomer engaging the 5′ displaced strand and anchoring onto the duplex may serve as a clamp that captures the displaced 5′ strand, and is hereafter referred to as the clamp protomer (Fig. 2c). By sequestering the displaced strand within its own channel and anchoring onto the duplex via its anchoring loop, the clamp protomer may physically prevent reannealing of the separated strands behind the advancing motor protomer, thereby enhancing the processivity of unwinding.

A fork-junction anchor from the clamp protomer couples ATP-driven translocation to strand separation

To understand how DruE couples ATP hydrolysis to DNA unwinding, we examined the nucleotide-binding site and DNA contacts at the fork junction. The nucleotide-binding site of the motor protomer lies in the cleft between RecA1 and RecA2 (Fig. 3a, b). The nucleotide and catalytic Mg^{2+} are coordinated by conserved motifs from both lobes. In RecA1, the Walker A motif (Motif I; Lys140) coordinates the phosphates, while the Q motif recognizes the adenine base through Gln116 hydrogen bonding and Tyr110/Tyr113 stacking. The arginine finger of Motif VI (Arg1241) reaches across the cleft from RecA2

(Fig. 3c). Alanine substitutions of Gln116, Lys140, or Arg1241 abolished both ATP hydrolysis and DNA unwinding, whereas the stacking tyrosines were largely dispensable (Fig. 3f, g), confirming the catalytic essentiality of the conserved SF2 motifs.

Beyond the nucleotide-binding site, the structure reveals protein–DNA contacts at the fork junction, mediated by two structural elements inserted within RecA1 of the clamp protomer (Fig. 3a). The anchoring loop (Anc-L) contacts the duplex arm through Lys176 and Arg178 (Fig. 3d); alanine substitutions of these residues caused only modest reductions in unwinding (Fig. 3h), suggesting that duplex contacts contribute to, but are not essential for, strand separation. Adjacent to Anc-L, the α-helical insertion (α-Ins) is positioned directly at the fork junction, where it contacts the branch point through Lys261 and the displaced strand through Arg269 (Fig. 3e). From the opposite face, residues Arg1949 and Arg1988 from ZBM3 provide additional contacts to the DNA at the junction. Together, α-Ins and ZBM3 form a composite structural element that straddles the fork junction. R269A, R1949A, and R1988A each produced only minor defects in unwinding, whereas K261A completely abolished strand separation while retaining wild-type ATPase activity (Fig. 3h, i). This uncoupling demonstrates that Lys261 is the critical functional residue within the α-Ins element, suggesting that α-Ins of the clamp protomer functions as a fork-junction wedge, analogous to the separation pins of SF1/SF2 helicases, converting motor-driven translocation into the force required to separate the duplex. Notably, whereas the separation pins of canonical SF1/SF2 helicases reside within the translocating subunit itself[23], the fork-junction wedge of DruE is contributed by the clamp protomer, suggesting that productive strand separation requires cooperation between the two protomers.

Two dimer interfaces with distinct functional contributions

The preceding analysis revealed that strand separation requires functional elements distributed across both protomers, translocation by the motor protomer and a fork-junction wedge from the clamp protomer. This interdependence suggests that the dimer interface is critical for DruE activity. To test this, we investigated how the dimer interface contributes to DruE activity. The DruE dimer interface is formed by the MarR-like domains of the two protomers, which contact each other through two distinct regions: a peripheral Interface I and a more deeply buried, central Interface II (Fig. 4a, b). Interface I consists of a hydrogen-bond network between antiparallel α-helices, one from each MarR-like domain, involving Glu880 and Lys885 (Fig. 4c). Interface II forms the central contact between the two MarR-like domains, involving His966 and Lys1033 (Fig. 4d).

Mutational analysis revealed distinct functions for the two interfaces. Disruption of Interface I (E880A, K885A) left DNA unwinding largely intact but increased ATPase activity above the wild-type level (Fig. 4e, f), suggesting that Interface I contributes to regulating the ATPase activity of the DruE dimer. In contrast, the Interface II substitution K1033A abolished unwinding while leaving ATPase activity largely unaffected (Fig. 4e, f). This uncoupling phenotype resembles that of the fork-junction mutant K261A, but the underlying mechanism is distinct: whereas K261A removes a direct protein–DNA contact at the fork, K1033A disrupts inter-protomer communication without affecting the catalytic site or DNA-binding interface. The loss of unwinding therefore indicates that coordination between the two protomers, mediated through the MarR-like domains, is essential for productive strand separation. Together, these data reveal that the two interfaces serve different roles: Interface I modulates ATPase activity, whereas Interface II mediates the

inter-protomer coupling required to coordinate the motor and clamp protomers during strand separation.

Conformational states of the DruE dimer define an asymmetric translocation cycle

Having established that the two protomers play distinct roles and that their coordination through the dimer interface is essential for unwinding, we next asked how the motor and clamp protomers cycle through conformational states during translocation. The seven cryo-EM reconstructions capture DruE in an apo (DNA-free, nucleotide-free) reference state (State I) and six DNA-bound states (States II–VII, Fig. 2a; Fig. S8a–g; Supplementary Movie 1), sampling different combinations of nucleotide occupancy and DNA engagement in the motor and clamp protomers. Because these are static snapshots rather than time-resolved observations, the conformational trajectory described below is inferred from structural comparison rather than directly observed.

In States I–IV, the clamp protomer remains nucleotide-free and conformationally unchanged, allowing us to track the conformational cycle of the motor protomer alone (Fig. 5a–d; Fig. S8a–d; Supplementary Movie 2). In the apo state (State I), a C-terminal module spanning the OB, ZBM3, CON, and DUF1998/ZBM4 domains (residues 1416–1721) is ordered and closes over the central channel (Fig. 5a). Upon ssDNA binding to the motor protomer (State II), this module becomes disordered, opening the channel to accommodate the tracking strand (Fig. 5b). Despite this disorder, the tracking strand is held in register by Arg785 within a basic-residue-rich loop of ZBM1, which contacts the substrate through electrostatic interactions and hydrogen bonds (Fig. 5e). This anchoring interaction appears critical for maintaining the motor protomer's grip on the tracking strand when the channel is open. Consistent with this role, an R785A substitution abolished

unwinding without reducing ATPase activity (Fig. 5h, i), indicating that loss of this contact uncouples translocation from strand separation. In State III (AMPPNP-bound), the module becomes stably ordered once more and recloses over the tracking strand, enclosing the ssDNA within the central channel. We therefore term this module the lid (Fig. 5c). Concurrently, RecA1 shifts toward the DNA-exit side of the channel (Fig. 5f), a conformational change consistent with the power stroke described for canonical SF2 helicases[24]. State IV (ADP-bound) is nearly identical to State III (overall Cα RMSD of 0.508 Å; Fig. S8h), with one notable exception: a loop at the N-terminal edge of the lid (residues 1419–1422) undergoes a conformational switch. In the AMPPNP state, Arg1422 hydrogen-bonds to Glu1501 in ZBM3. In the ADP state, the loop swings so that Arg1422 instead contacts Gln1666 in DUF1998/ZBM4 (Fig. 5g). Because this switch correlates with the transition from the AMPPNP to the ADP state, we propose that ATP hydrolysis triggers a ratchet-like conformational change that locks the forward progress achieved during the preceding power stroke, thereby ensuring unidirectional translocation. Consistent with a functional role for this loop, R1422A and P1420A abolished unwinding, whereas M1419A had little effect (Fig. 5h, i).

States V–VII capture conformations in which the clamp protomer has engaged the 5′ displaced strand and bound nucleotide (AMPPNP in States V and VI, ADP in State VII). In States I–IV, the clamp protomer is nucleotide-free and its central channel is occluded(Fig. S8a–d, i). By contrast, in States V–VII, nucleotide binding and displaced-strand engagement widen the channel, and a greater length of the duplex arm is resolved (Fig. S8e–g, j). The anchoring loop of the clamp protomer now contacts the duplex stem, an interaction absent from States II–IV (Fig. S8, b–d). Nucleotide also reshapes its

binding pocket (Fig. S8k), suggesting that nucleotide stabilizes the displaced-strand-bound conformation and strengthens the grip on the substrate. Importantly, across States V–VII the motor protomer reproduces the same lid cycle observed in States II–IV, with the lid open when nucleotide-free (State V) and closed when AMPPNP- (State VI) or ADP-bound (State VII), independently of the nucleotide state of the clamp protomer (Fig. S8b–g). The two protomers are therefore gated independently rather than operating in synchrony.

Together, these observations suggest the following translocation cycle for the motor protomer. In the resting state, the lid is closed over an empty channel. ssDNA binding opens the lid, allowing the tracking strand to enter. ATP binding recloses the lid and drives a conformational change in the RecA domains consistent with a power stroke. ATP hydrolysis triggers the Arg1422 ratchet, locking the forward progress. ADP release then reopens the lid, resetting the motor for the next cycle. Throughout this process, the clamp protomer maintains its grip on the displaced strand and the adjacent duplex, physically preventing reannealing behind the advancing motor and thereby enhancing processivity. The DruE dimer thus operates as an asymmetric machine in which the motor and clamp protomers cooperate to achieve processive duplex unwinding.

Discussion

The Druantia antiphage defence systems are widespread in bacteria, yet the type II system has remained functionally and structurally uncharacterized. Here, we demonstrate that the type II effector DruE is a 3′-to-5′ helicase that assembles as a constitutive asymmetric homodimer, in which a motor protomer and a clamp protomer perform complementary roles during DNA unwinding. Seven cryo-EM structures

spanning substrate-free through nucleotide-bound states, combined with biochemical analyses, enable us to propose a mechanochemical model for directional unwinding by this immune helicase.

A mechanochemical model for DruE-mediated DNA unwinding. Our structural and biochemical analyses reveal that the type II Druantia effector DruE operates as an asymmetric homodimer in which two sequence-identical protomers adopt distinct functional roles during DNA unwinding. The seven cryo-EM structures, spanning the substrate-free state through DNA loading to nucleotide-dependent conformational cycling, allow us to propose a mechanochemical model for directional DNA unwinding by an immune helicase (Fig. 6a). The motor protomer serves as the translocating engine. In the absence of nucleotide, the 3′ tracking strand threads into the central channel and triggers a large conformational rearrangement in ZBM1, while the C-terminal lid module remains disordered (State II). Nucleotide binding closes the lid over the tracking strand and induces a forward displacement of the RecA1 domain that is consistent with a power stroke that may advance the substrate along the unwinding path (State III). The transition from the AMPPNP-bound to the ADP-bound state is accompanied by a conformational switch in the Arg1422-containing loop at the lid margin (States III to IV), which we propose biases translocation directionality by acting as a ratchet. The clamp protomer performs a distinct function. Upon capturing the 5′ displaced strand (States V–VII), its C-terminal region undergoes a large conformational change that widens the DNA-binding channel and forms a clamp-like grip on the displaced strand and adjacent duplex. Nucleotide binding to the clamp protomer stabilizes this conformation, suggesting that it enhances the processivity of the complex by preventing substrate dissociation and strand

reannealing. Importantly, the lid of the motor protomer cycles between open and closed states independently of the nucleotide occupancy of the clamp protomer, indicating that the two protomers are gated independently. Two additional structural elements contribute to the coupling of ATP hydrolysis to productive unwinding. The α-Ins element, positioned at the fork junction in the clamp protomer, functions as a wedge that is essential for strand separation but dispensable for ATPase activity. Notably, whereas the separation pins of canonical SF1 and SF2 helicases reside within the translocating subunit itself[23,25,26], the fork-junction wedge of DruE is contributed by the clamp protomer, indicating that productive strand separation in DruE requires inter-protomer cooperation between the translocation force generated by the motor and the physical wedge provided by the clamp. Consistent with this, the central dimer Interface II, mediated by the MarR-like domains, is similarly required for unwinding but not for ATP hydrolysis, confirming that inter-protomer communication through this contact is essential for productive strand separation.

Comparison with other immune helicase systems. The rapidly expanding inventory of helicase-centred defence systems now includes Hachiman, DISARM, and Druantia, among others, each built around an SF1 or SF2 helicase but employing distinct architectures and substrate specificities[14–18]. The Hachiman helicase HamB, a Ski2-like enzyme, also recognizes 3′ single-stranded overhangs. However, HamB operates as a monomer whose mechanochemical ratcheting allosterically activates a separate nuclease, HamA, leading to indiscriminate DNA degradation and abortive infection[14]. By contrast, DruE functions as a stable dimer and lacks an associated nuclease, suggesting a fundamentally different downstream mechanism. The DISARM helicase DrmAB recognizes 5′ overhangs rather than 3′ overhangs and is held in an autoinhibited state by

a trigger loop that must be displaced for activation[16]. DruE does not exhibit a comparable autoinhibited conformation in any of the seven structures reported here. Although the lid is closed in the apo state, this closure reflects a default resting conformation that is remodelled upon substrate binding, rather than an inhibitory mechanism requiring a specific activation signal. Whether regulation of type II Druantia is imposed by the accessory components, by substrate availability, or by additional cellular factors remains to be tested.

A particularly informative comparison involves the type III Druantia system, for which multiple recent studies have provided structural and functional insights[19,27,28]. Several groups have independently determined cryo-EM structures of type III DruE and report that it also assembles as an asymmetric dimer with 3′-to-5′ unwinding polarity, suggesting that asymmetric dimerization is a conserved feature of YprA-family immune helicases rather than a property unique to the type II system[27,28]. However, the two subtypes differ in important respects. Type III DruE contains C-terminal PLD-like nuclease domains that are absent from type II DruE, making type III DruE a bifunctional helicase-nuclease effector capable of directly degrading DNA substrates[27,28]. In the type II system, DruE lacks intrinsic nuclease activity, and how its unwinding activity is converted into phage restriction remains an open question. The accessory components also diverge: type III systems encode a single partner, DruH, which has been characterized as an ssDNA-binding protein, a 3′ DNA end-processing exonuclease, or a metabolic sensor depending on the system and study[19,27,28], whereas type II systems encode three distinct accessory proteins (DruM, DruF, and DruG) whose functions remain to be defined. Furthermore, whereas some type III studies report that the DruE dimer undergoes activation-coupled

remodeling or transitions between monomeric and dimeric states[27,28], the type II DruE dimer described here is constitutive and present in all seven reconstructions, including the substrate-free apo state. In addition, recent work has shown that type III Druantia systems can synergize with co-localized defence systems such as Zorya II through shared DNA-processing intermediates dependent on the RecBCD complex[29,30], raising the possibility that type II Druantia may similarly cooperate with neighbouring defence loci, although this has not yet been tested. Together, these comparisons suggest that while the YprA-family helicase core and its asymmetric dimeric architecture are broadly conserved, the Druantia subtypes have diverged substantially in their effector mechanisms, regulatory strategies, and modes of oligomeric control.

Biological implications and accessory protein function. The biochemical preference of DruE for 3′-ended and fork-like DNA substrates is consistent with the recognition of structures that arise during phage genome replication, including cohesive-end processing, rolling-circle intermediates, and stalled or branched replication forks[31,32]. We therefore propose that DruE targets vulnerable stages of the phage replication cycle through ATP-dependent unwinding (Fig. 6b). However, such fork-like structures can also arise during normal host DNA metabolism, raising the question of how the system avoids self-toxicity. Our genetic analyses provide an initial clue. Deletion of *druE* alleviates MMC-induced toxicity in *P. protegens* Pf-5, whereas deletion of *druM*, *druF*, or *druG* exacerbates growth defects under MMC treatment. These observations suggest that DruM, DruF, and DruG are required to maintain host fitness under DNA-damaging conditions and may help tune or constrain DruE-associated activity. The precise molecular functions of these accessory components remain to be established through biochemical reconstitution of the full type

II complex.

Limitations. Several caveats should be noted. All structures were determined with nucleotide analogs (AMPPNP) or hydrolysis products (ADP), and the conformational trajectory is inferred from comparison of static snapshots rather than from time-resolved observation. DruE alone confers limited protection against a subset of coliphages in heterologous expression, and the full type II system could not be reconstituted because DruF and DruG accumulated in the insoluble fraction. Furthermore, no cognate phages have been identified for *P. protegens* Pf-5, precluding direct assessment of type II Druantia-mediated defence in the native host. Finally, how the DNA unwinding activity of DruE is converted into phage restriction remains unclear.

Materials and Methods

Experimental models and bacterial strains

For standard cultivation, all *Escherichia coli* strains were grown in Luria-Bertani (LB) medium at 37°C with shaking at 220 r.p.m. Antibiotics were supplemented as required for plasmid maintenance (e.g., ampicillin at 100 μg/mL). Bacterial strains were stored at -80°C as 25% (v/v) glycerol stocks. *E. coli* DH5α was used for plasmid cloning and amplification, whereas *E. coli* BL21 (DE3) and *E. coli* BL21 were employed for protein expression and phage infection assays, respectively. Phages T1, T4, T5, T7, and λ were used in this study. Phage propagation followed standard protocols, typically infecting logarithmically growing host cells in LB medium at 37°C with an initial multiplicity of infection (MOI) of 0.1. Phage titers were determined using the double-layer agar plate method. All strains, plasmids, and phages used in this study are detailed in Supplementary Table S6.

Construction of mutant strains

The in-frame deletion mutants were generated using a two-step homologous recombination approach as previously described[33]. Briefly, ~1 kb flanking regions upstream and downstream of the target gene were amplified by PCR using high-fidelity DNA polymerase. These two fragments were fused by overlap extension PCR and then cloned into the suicide vector pK18mobsacB. The resulting recombinant plasmid was transformed into *E. coli* WM3064 and subsequently transferred into the recipient strain via conjugation on LB agar supplemented with 0.3 mM DAP. The single-crossover transconjugants were first selected on LB agar containing kanamycin and then cultured in LB broth without antibiotics to allow for the second crossover. Subsequently, the cultures were spread onto LB agar supplemented with 10% sucrose to counter-select against vector retention via the *sacB* gene; sucrose-resistant colonies were screened and successful deletion mutants were validated by PCR using target gene primers.

Identification and visualization of Druantia loci

Based on DefenseFinder[34] annotations, Druantia loci and their neighbouring defence systems were identified in the genomes of *Serratia fonticola* (GCF_005489985.1), *Pseudomonas protegens* Pf-5 (GCF_000012265.1), *Klebsiella michiganensis* (GCF_002025225.1), and *Metabacillus litoralis* SW-211 (GCF_007994985.1). Genomic operons were visualized using the Python library dna_features_viewer[35], coupled with pandas for data processing and matplotlib for auxiliary plotting.

Plasmid construction and protein purification

All plasmids generated in this study were constructed using PCR, gel extraction (Omega Bio-tek, D2500-02), and either Gibson assembly[36] or Golden Gate assembly[37]. Genomic

DNA from *P. protegens* Pf-5, extracted using the TIANGEN Bacterial Genomic DNA Extraction Kit, served as the template for amplifying wild-type Druantia genes. Wild-type *druE* and the indicated *druE* point mutants were cloned into the respective expression vectors; all primers and constructs are listed in Supplementary Tables S4 and S6.

For protein expression, *E. coli* BL21 (DE3) cells harboring the pETDuet-1-*druE* plasmid were inoculated into 1 L of LB medium and cultured at 37°C until the OD_{600} reached 0.6–0.8. Protein expression was induced with 0.5 mM IPTG at 16°C overnight (16 hours). Cells were harvested, resuspended in lysis buffer (20 mM Tris-HCl pH 8.0, 500 mM NaCl), and lysed via sonication (70% amplitude, 1 s on, 2 s off, 20 min total). Following high-speed centrifugation (12,000 × g, 45 min), the supernatant was collected and applied to Strep-Tactin 4FF affinity resin (Smart Lifesciences, Changzhou, China). After washing out non-specifically bound proteins, the target protein was eluted using a buffer supplemented with 2.5 mM desthiobiotin. The eluate was then concentrated and injected onto a pre-equilibrated Superdex 200 10/300 GL size-exclusion chromatography column (Cytiva) for polishing, using chromatography buffer (20 mM Tris-HCl pH 8.0, 150 mM NaCl). The oligomeric state was evaluated based on the elution volume (indicating a homodimer of approximately 400 kDa). The peak fractions were pooled, flash-frozen in liquid nitrogen, and stored at -80°C. Mutant proteins were purified following the identical protocol as the wild type.

Efficiency of plating determination

To determine the efficiency of plating (EOP), phages were plated on induced strains expressing DruE and compared with plaques formed on the empty-vector BL21 control. Briefly, 200 μL of bacterial culture was mixed with 50–150 PFU and 4.5 mL of 0.6% LBA

prewarmed to 45°C. The mixture was poured onto an LBA plate to form a bacterial lawn. After overnight incubation at 37°C, EOP was calculated by dividing the number of plaques on each test strain by the number of plaques on the control strain.

DNA substrate preparation

All single-stranded oligonucleotides, including those with 5′-FAM fluorescent modifications, were synthesized by GENEWIZ (Tianjin, China). To prepare various double-stranded DNA (dsDNA) substrates (e.g., blunt-ended, 3′-overhang, 5′-overhang, and Y-fork), single-stranded oligonucleotides were mixed with equimolar or a 1.5-fold excess of their complementary strands in annealing buffer (20 mM Tris-HCl pH 7.5, 50 mM NaCl, 5 mM $MgCl_2$). Annealing was facilitated by heating the mixture to 95°C for 5 min, followed by a gradual cooling to 25°C over 110 min. The purity of the annealed products was verified by 8% native polyacrylamide gel electrophoresis (PAGE)[14]. Sequences of all substrates are detailed in Supplementary Table S5.

Cryo-EM sample preparation and data collection

To capture the DruE complex during DNA unwinding, a Y-fork DNA construct was designed, comprising a 19-bp stem region, a 6-nt 5′-overhang, and a 21-nt 3′-overhang [34,35] (Table S5, Fig. S4a). This specific substrate was selected as it has been widely utilized to trap unwinding intermediates of bacterial SF2 helicase complexes. Purified DruE (5 μM) was incubated with a 10-fold molar excess of DNA substrate (50 μM) and either ADP or AMPPNP at a final concentration of 0.5 mM (100-fold molar excess; Macklin Biochemical, Shanghai, China). Following a 30-minute incubation at room temperature (~25°C), 4 μL of the DruE–DNA–ADP mixture was applied to glow-discharged holey carbon grids (Copper, 300 mesh, R1.2/1.3, Quantifoil). The grids were blotted for 4 s at

4°C under 100% humidity using a Vitrobot Mark IV (FEI Company) and rapidly plunge-frozen in liquid ethane.

Cryo-EM data were acquired on a Krios G4 transmission electron microscope operating at 300 kV, equipped with a Falcon4i direct electron detector and a Selectris X energy filter (slit width: 10 eV). Movie stacks were collected in electron event representation (EER) mode using EPU software (Thermo Fisher Scientific), with a total electron dose of 50 $e^{-}/Å^{2}$ and a defocus range of -0.8 µm to -1.6 µm. Sample preparation and data collection for the DruE–DNA–AMPPNP complex were performed identically to those for the ADP state.

Cryo-EM image processing

All cryo-EM data processing was performed in cryoSPARC[38]. Preprocessing and particle picking: All datasets were collected with a pixel size of 0.96 Å/pixel. Beam-induced motion correction of movie stacks was performed using the Patch Motion Correction module, and contrast transfer function (CTF) parameters were estimated via Patch CTF Estimation. Initial particle picking was conducted using Blob Picker with an un-binned box size of 400 pixels, followed by 2D classification of 2× and 4× down-sampled particles to generate reference templates. Subsequently, template-based picking was executed on the motion-corrected and CTF-estimated micrographs utilizing Template Picker.

Processing of the DruE–DNA–ADP complex: For this dataset (Fig. S4), a total of 4,571 movie stacks were collected. Template Picker yielded an initial set of 2,542,668 particles. These particles were subjected to *ab initio* reconstruction (C1 symmetry), generating 5 classes. To eliminate "junk" classes, three rounds of heterogeneous refinement (box size 128 pixels, forced hard classification) were performed. This process isolated 417,803

high-quality 'passthrough' particles, yielding a consensus reconstruction with a gold-standard Fourier shell correlation (GSFSC) overall resolution of 3.31 Å. The consensus particle set was further subjected to non-uniform refinement, incorporating per-particle defocus optimization, global CTF refinement (tilt, trefoil, and spherical aberration), noise model initialization from images, and local motion correction. A subsequent round of heterogeneous refinement (box size 128 pixels, initial resolution 6 Å) successfully classified the particles into three distinct conformational states: State I (27,065 particles, 3.64 Å), State IV (73,269 particles, 3.45 Å), and State VII (210,656 particles, 3.29 Å).

Processing of the DruE–DNA–AMPPNP complex: For this dataset (Fig. S5), 6,752 movie stacks were collected. Following a parallel processing pipeline, 1,928,979 particles were initially picked. After *ab initio* reconstruction (5 classes) and three rounds of heterogeneous refinement to filter out "junk" particles, 616,796 high-quality particles were retained, yielding a consensus reconstruction at 3.26 Å resolution. Following an identical non-uniform refinement strategy, heterogeneous refinement classified the dataset into four distinct states: State II (233,472 particles, 3.28 Å), State III (136,706 particles, 3.36 Å), State V (138,033 particles, 3.45 Å), and State VI (50,310 particles, 3.58 Å).

Local refinement and post-processing: To enhance the local density quality surrounding the ATP-binding site, local refinement was performed using a mask focused on this region. The resulting refined 3D volumes were subsequently post-processed using EMReady2[39] to facilitate model building.

Model building and refinement

The initial model of DruE was generated using AlphaFold2[40]. For model building, the predicted model was rigid-body fitted into the experimental cryo-EM density maps using

the fitmap tool in UCSF ChimeraX v1.10.1[41]. Given the significant conformational disparities between the prediction and the experimental structure, multiple rounds of manual, iterative building were performed utilizing Coot[42], the ISOLDE plugin[43], and Phenix[44]. This initially refined DruE structure subsequently served as the baseline model for all other conformational states. The DNA substrate, zinc ion (Zn^{2+}), and nucleotide ligands (ADP or AMPPNP) were built *de novo* in Coot based on the experimental density. Finally, all atomic models underwent real-space refinement using phenix.real_space_refine, and the overall geometric quality was evaluated using MolProbity[45].

NTPase activity assays

The ATPase activity of DruE was evaluated by quantifying the release of inorganic phosphate using a Malachite Green Phosphate Assay Kit (Beyotime) according to the manufacturer's instructions[46]. Reactions were carried out in a buffer containing 20 mM Tris-HCl pH 7.5, 50 mM KCl, 2 mM $MgCl_2$, and 1 mM DTT. Assays were performed in transparent-bottom, black 96-well plates. DruE was diluted to a final concentration of 40 nM, and the nucleic acid substrate (Table S5) was diluted to 100 nM (or plasmid DNA to a final concentration of 4 ng/μL), in a total reaction volume of 10 μL. The reaction mixture was pre-incubated at room temperature for 5 min. ATP (Macklin Biochemical, Shanghai, China) was then added to a final concentration of 1 mM to initiate the reaction, followed by incubation at 37°C for 30 min. The reaction was quenched by the addition of the activated Malachite Green reagent. After a 30-minute colorimetric development in the dark at room temperature, the absorbance at 620 nm was measured using a BioTek microplate reader. Phosphate release was quantified by interpolation from a standard

curve of free phosphate. Oligonucleotide substrates are modified from Domgaard et al[47].

Gel-shift helicase unwinding assays

Helicase unwinding reactions were performed in Isothermal Amplification Buffer (IAB; 20 mM Tris-HCl, 10 mM $(NH_4)_2SO_4$, 50 mM KCl, 2 mM $MgSO_4$, and 0.1% Tween® 20; pH 8.8 at 25°C) at 30°C. DruE (100 nM) was pre-incubated with 20 nM of fluorescently labeled DNA substrate (Supplementary Table S5) for 5 min. The reaction was initiated by the addition of 1 mM ATP or AMPPNP (Macklin Biochemical). At 20 min, aliquots were transferred to ice and quenched with a STOP buffer (containing 0.4 U Proteinase K, 18 mM EDTA, 0.36% SDS, and 9% glycerol). To prevent re-annealing of the unwound DNA strands, a 2-fold molar excess of unlabeled trap oligonucleotide (identical in sequence to the fluorescently labeled single strand) was added during the quenching step. For the fully unwound control (Boiled control), the substrate was boiled at 95°C for 5 min and loaded immediately. All samples were resolved on a 12% TBE polyacrylamide gel at 4°C until the bands were adequately separated. The gel was then scanned using a multifunctional laser imaging and automated gel excision system (Bio-Rad/BIO-LAB PharosFX), and images were exported with Image Lab software.

Construction of single-gene knockout mutants and phenotypic assays

To investigate the in vivo function of the Druantia system in its native host, *Pseudomonas protegens* Pf-5, in-frame deletion mutants of the four core genes (*druM, druF, druG,* and *druE*) were independently constructed using a two-step homologous recombination approach. Briefly, approximately 1-kb regions upstream and downstream of each target gene were amplified using a high-fidelity DNA polymerase, fused by overlap-extension PCR, and cloned into the suicide vector pK18mobsacB. The resulting recombinant

plasmids were introduced into *Escherichia coli* WM3064 and subsequently transferred into Pf-5 by conjugation on LB agar supplemented with 0.3 mM diaminopimelic acid (DAP). Single-crossover transconjugants were selected on LB agar containing kanamycin and cultured in antibiotic-free LB broth to facilitate the second crossover. Cultures were then plated on LB agar containing 10% sucrose to counter-select cells retaining the *sacB*-containing vector. Sucrose-resistant colonies were screened by PCR to confirm the successful generation of the Δ*druM*, Δ*druF*, Δ*druG*, and Δ*druE* mutants.

For phenotypic assays, the wild-type (WT) Pf-5 strain and the four knockout mutants were cultured overnight and subcultured 1:100 into fresh liquid medium. When the cultures reached an OD_{600} of 0.2, mitomycin C (MMC; Aladdin Biochemical Technology, Shanghai, China) was added to the treatment groups at a final concentration of 2 μg/mL, while the control groups received an equivalent volume of vehicle. The cultures were transferred to 96-well plates, and growth kinetics were continuously monitored by measuring OD_{600} with a BioTek microplate reader. All experiments were conducted using three independent biological replicates, and statistical analyses were performed using GraphPad Prism 9. Growth curves were analyzed by two-way repeated-measures ANOVA, followed by Dunnett's multiple-comparisons test to compare each single-gene deletion strain (Δ*druM*, Δ*druF*, Δ*druG*, and Δ*druE*) with the WT strain at each time point following MMC treatment.

Data Availability

All data supporting the findings of this study are available within the paper and its Supplementary Information. For the DruE–DNA–ADP complex, the cryo-EM density maps for the three conformational states (State I, State IV, and State VII) have been deposited in the Electron Microscopy Data Bank (EMDB) under accession codes EMD-

65815 (State I), EMD-65907 (State IV), and EMD-65816 (State VII); the corresponding atomic models have been deposited in the Protein Data Bank (PDB) under accession codes 9WAE (State I), 9WDV (State IV), and 9WAF (State VII). The consensus reconstruction density map is available under EMD-65895, and the locally refined maps for State I under EMD-65813 and EMD-65814.

For the DruE–DNA–AMPPNP complex, the density maps for the four states (State II, State III, State V, and State VI) are deposited under EMDB accession codes EMD-65906 (State II), EMD-65908 (State III), EMD-65901 (State V), and EMD-65910 (State VI); the corresponding PDB models are deposited under 9WDU (State II), 9WDW (State III), 9WDS (State V), and 9WDY (State VI). The consensus and locally refined maps for the State II state are deposited under EMD-65902, EMD-65903, and EMD-65904; and those for the State V state under EMD-65897, EMD-65898, and EMD-65899.

Acknowledgements

We gratefully acknowledge Dr. Gang Fu for technical support during cryo-EM image acquisition. We also thank the Structural Biology Core Facility at the Bio-Tech Center of SMART for technical assistance. Additionally, we acknowledge the Computing Labware for Electron Microscopy Visualization and Experimental Research (CLEVER) at SMART for support with data analysis. This study was supported by the Gansu Research Program (Grant No 22CX8NA001) and the National Natural Science Foundation of China (Grant No 31971422).

Author contributions

L.G. and Y.-X.H. conceived, initiated, and coordinated the project; J.H. and W.-W.K. prepared cryo-EM grids and collected the cryo-EM data; J.H. and Y.Y. built and refined

622 the structure model; X.Y. performed most of the biochemical and physiological
623 experiments; F.Y., P.L., H.F., and Z.C. assisted with part of the experiments; J.H., W.-
624 W.K., X.Y., L.G., and Y.-X.H. wrote the manuscript. All authors discussed the experiments
625 and results and read and approved the manuscript.

626 **Competing interests**

627 The authors declare no competing interests.

628 **Supplementary Movie Legends**

629 **Supplementary Movie 1.** Seven conformational states of the DruE dimer. Animation
630 comparing the cryo-EM reconstructions and fitted models for States I–VII, highlighting
631 nucleotide- and DNA-dependent changes in the motor and clamp protomers.

632 **Supplementary Movie 2.** Motor-protomer conformational cycle of DruE. Animation
633 illustrating the transition from State I to State IV in the motor protomer, including ssDNA
634 binding, ATP-associated lid closure and power-stroke-like movement, and the ADP-
635 associated R1422 ratchet switch.

636

637 **Figure Legends**

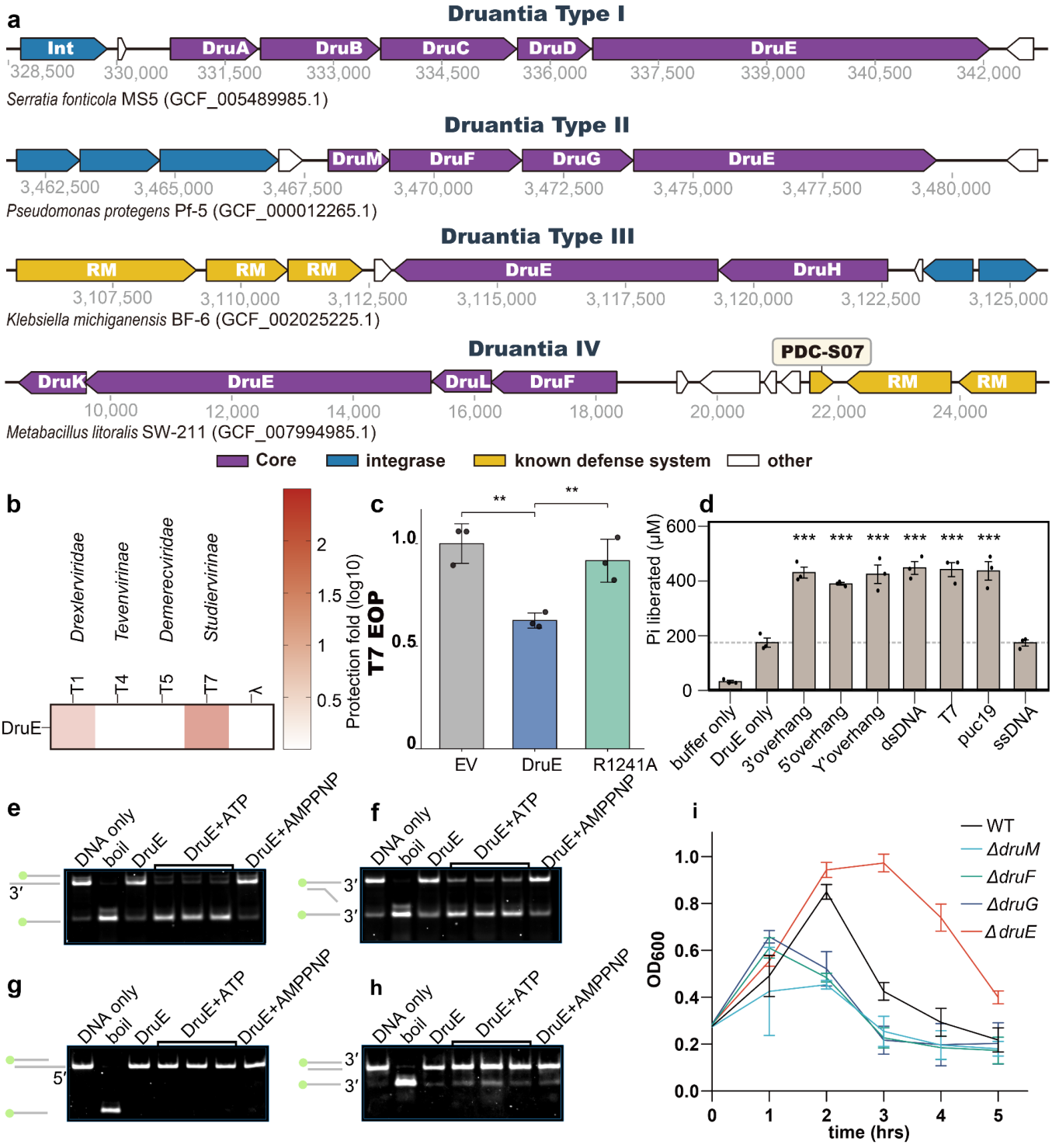

Figure 1. Genomic organization, antiphage activity and biochemical characterization of type II Druantia DruE. (a) Schematic representation of representative genomic loci for the four major Druantia subtypes (Types I–IV). Genes are coloured by functional category: purple, core Druantia genes including the conserved SF2 helicase DruE; blue, integrases; yellow, known defence systems; white, other neighbouring genes. Bacterial strains and NCBI assembly accessions are indicated below each locus. (b) Phage protection profile of *Pseudomonas protegens* Pf-5 DruE expressed in *Escherichia coli* against five bacteriophages (T1, T4, T5, T7 and λ). The heat map indicates log10 protection fold. (c) Efficiency of plating (EOP) of phage T7 on *E. coli* expressing empty vector (EV), wild-type DruE or the catalytic-site mutant DruE R1241A. Data are from three independent biological replicates; statistical significance was assessed using a two-tailed unpaired Student's t-test. (d) ATPase activity of purified DruE in the absence or presence of the indicated DNA substrates, quantified by measuring released inorganic phosphate (Pi). Bars represent the mean ± s.d. from three independent experiments. (e–h) Native PAGE-based helicase assays using a 3′ overhang substrate (e), a Y'overhang substrate (f), a 5′ overhang substrate (g) or a blunt-ended duplex substrate (h). Reactions contained DNA alone, boiled substrate, DruE without nucleotide, DruE with ATP, or DruE with the non-hydrolysable ATP analogue AMPPNP, as indicated. (i) Growth curves of *P. protegens* Pf-5 wild type (WT) and single-gene deletion strains (Δ*druM*, Δ*druF*, Δ*druG* and Δ*druE*) following mitomycin C (MMC) treatment. OD_{600} was monitored over 5 h. Statistical significance is indicated where shown: *P < 0.05, **P < 0.01 and ***P < 0.001.

660

a

Motor protomer \ Clamp protomer	Apo	5′ DNA–AMPPNP-bound	5′ DNA–ADP-bound
Apo	State I	N/A	N/A
3′ DNA-bound	State II	State V	N/A
3′ DNA–AMPPNP-bound	State III	State VI	N/A
3′ DNA–ADP-bound	State IV	N/A	State VII

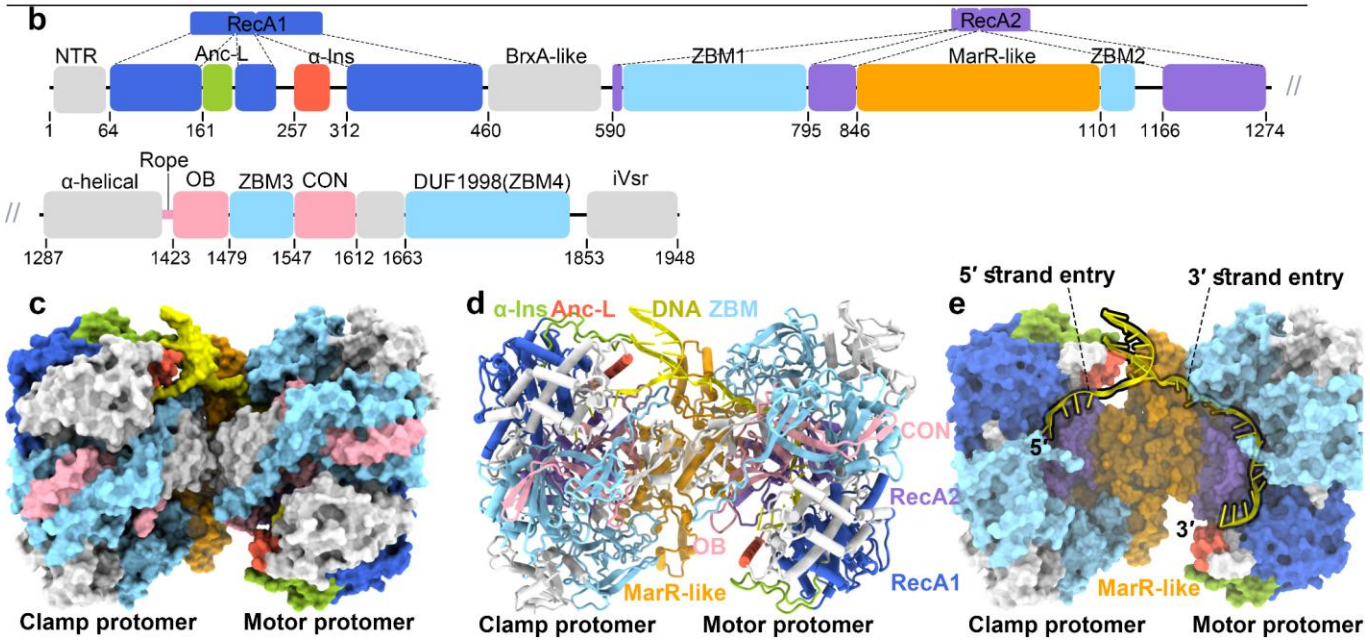

661

Figure 2. Domain architecture and asymmetric dimeric structure of DruE bound to forked DNA. (a) Summary of the seven conformational states captured in this study, defined by the DNA- and nucleotide-binding status of the motor and clamp protomers. (b) Linear domain organization of DruE. The catalytic core comprises two discontinuous RecA-like domains, RecA1 and RecA2, interrupted by large insertions including the anchoring loop (Anc-L), α-helical insertion (α-Ins), BrxA-like domain, zinc-binding modules (ZBM1 and ZBM2) and a MarR-like domain. The C-terminal region contains an α-helical domain, OB fold, ZBM3, connector (CON) domain, DUF1998/ZBM4 and iVsr domain. (c) Surface representation of the asymmetric DruE homodimer bound to forked DNA, highlighting the clamp protomer and motor protomer. (d) Ribbon representation of the DNA-bound dimer, showing the arrangement of the helicase core, accessory domains and forked DNA. (e) Surface view showing that the 5′ displaced strand and 3′ tracking strand enter distinct channels on opposite sides of the DruE dimer. See Supplementary Movie 1 for a visual comparison of the seven conformational states.

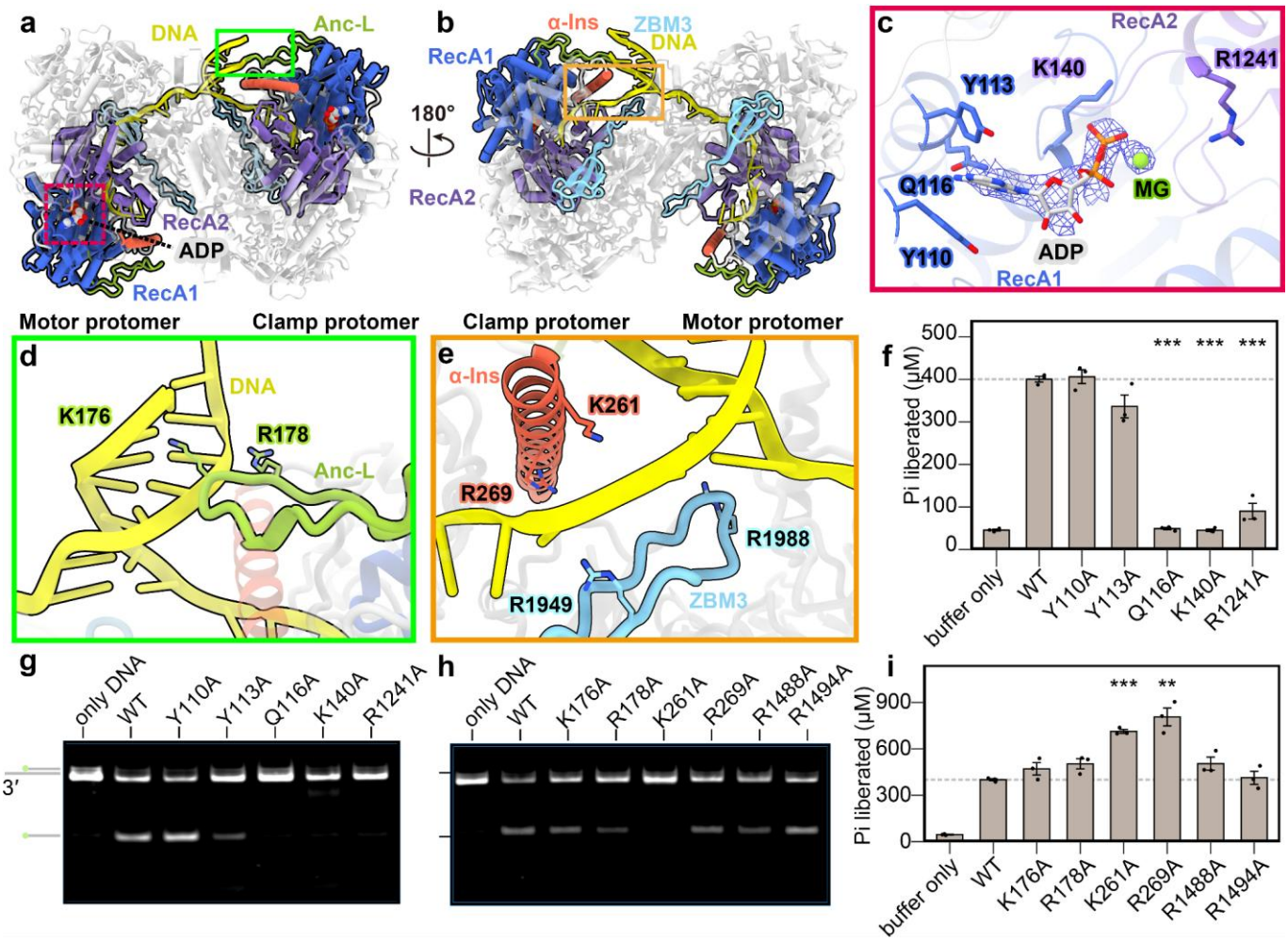

676

Figure 3. Nucleotide recognition and DNA contacts at the fork junction. (a,b) Overall views of the DNA-bound DruE dimer, shown in two orientations related by a 180° rotation. The motor and clamp protomers are indicated, and boxed regions mark the nucleotide-binding pocket and fork-junction contacts. (c) Close-up view of the ADP-binding pocket in the motor protomer, with the cryo-EM density for ADP and Mg^{2+} shown as a blue mesh. Y110, Y113, Q116, K140 and R1241 are shown as sticks. (d) Close-up view of the anchoring loop (Anc-L) contacting the duplex arm through K176 and R178. (e) Close-up view of the fork-junction interface, where K261 and R269 from ⟨-Ins and R1949 and R1988 from ZBM3 contact the forked DNA. (f) DNA-stimulated ATPase activities of WT DruE and nucleotide-binding-site mutants. (g,h) Native PAGE-based helicase assays comparing WT DruE with alanine-substitution mutants in the nucleotide-binding pocket (g) or DNA-binding interface (h) DNA alone serves as the negative control. (i) DNA-stimulated ATPase activities of WT DruE and DNA-interface mutants. Data in f and i are from three independent experiments; statistical significance relative to WT was assessed using two-tailed unpaired Student's t-tests. Statistical significance is indicated as **P < 0.01 and ***P < 0.001.

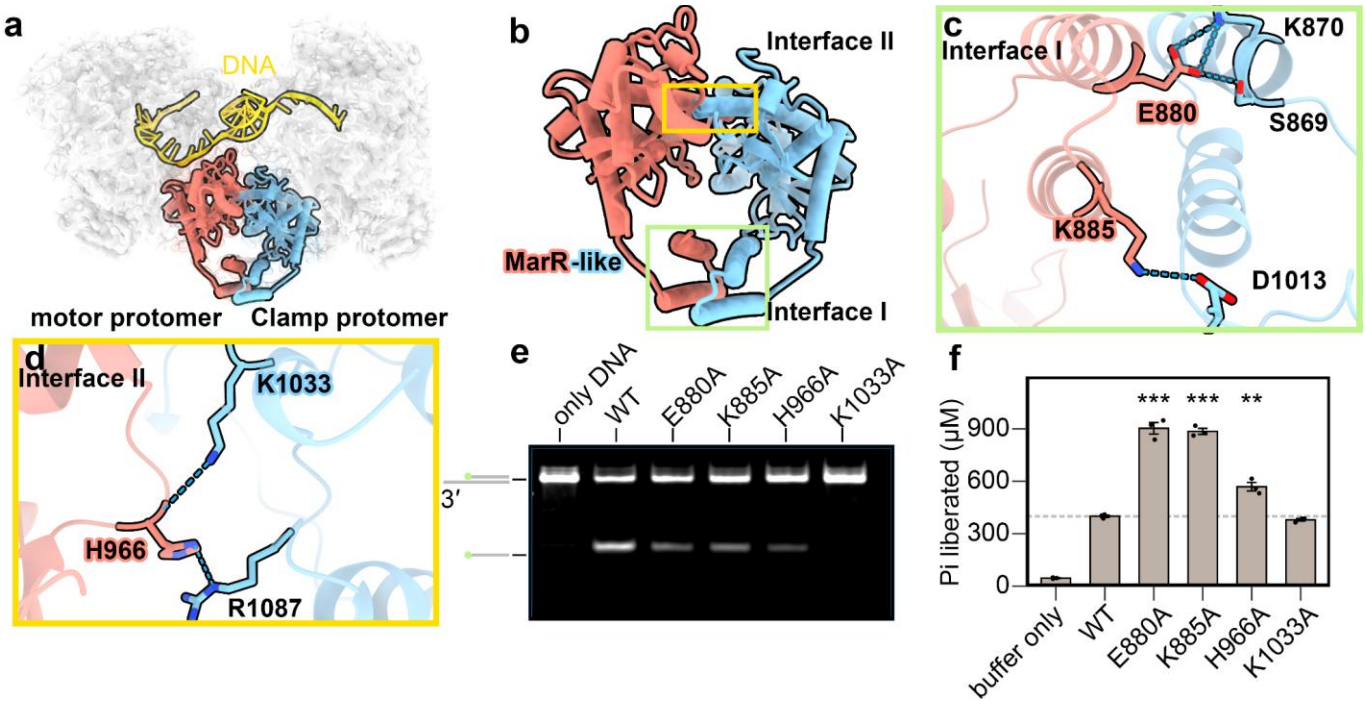

693

694 **Figure 4.** Structural and functional characterization of the DruE dimer interfaces. (a) Cryo-
695 EM density map of the DNA-bound DruE dimer, showing the motor protomer, clamp
696 protomer and forked DNA. (b) Cartoon representation of the MarR-like dimer interface,
697 highlighting two inter-protomer contact regions, peripheral Interface I and central Interface
698 II. (c) Close-up view of Interface I, showing interactions involving S869, K870, E880, K885
699 and D1013. Hydrogen bonds and electrostatic interactions are indicated by dashed lines.
700 (d) Close-up view of Interface II, showing contacts involving H966, K1033 and R1087. (e)
701 Native PAGE-based helicase assays comparing the 3′-to-5′ DNA-unwinding activities of
702 WT DruE and the indicated dimer-interface mutants. DNA alone serves as the negative
703 control. (f) DNA-stimulated ATPase activities of WT DruE and interface mutants. Data in
704 f are from three independent experiments; statistical significance relative to WT was
705 assessed using two-tailed unpaired Student's t-tests. Statistical significance is indicated
706 as **P < 0.01 and ***P < 0.001.

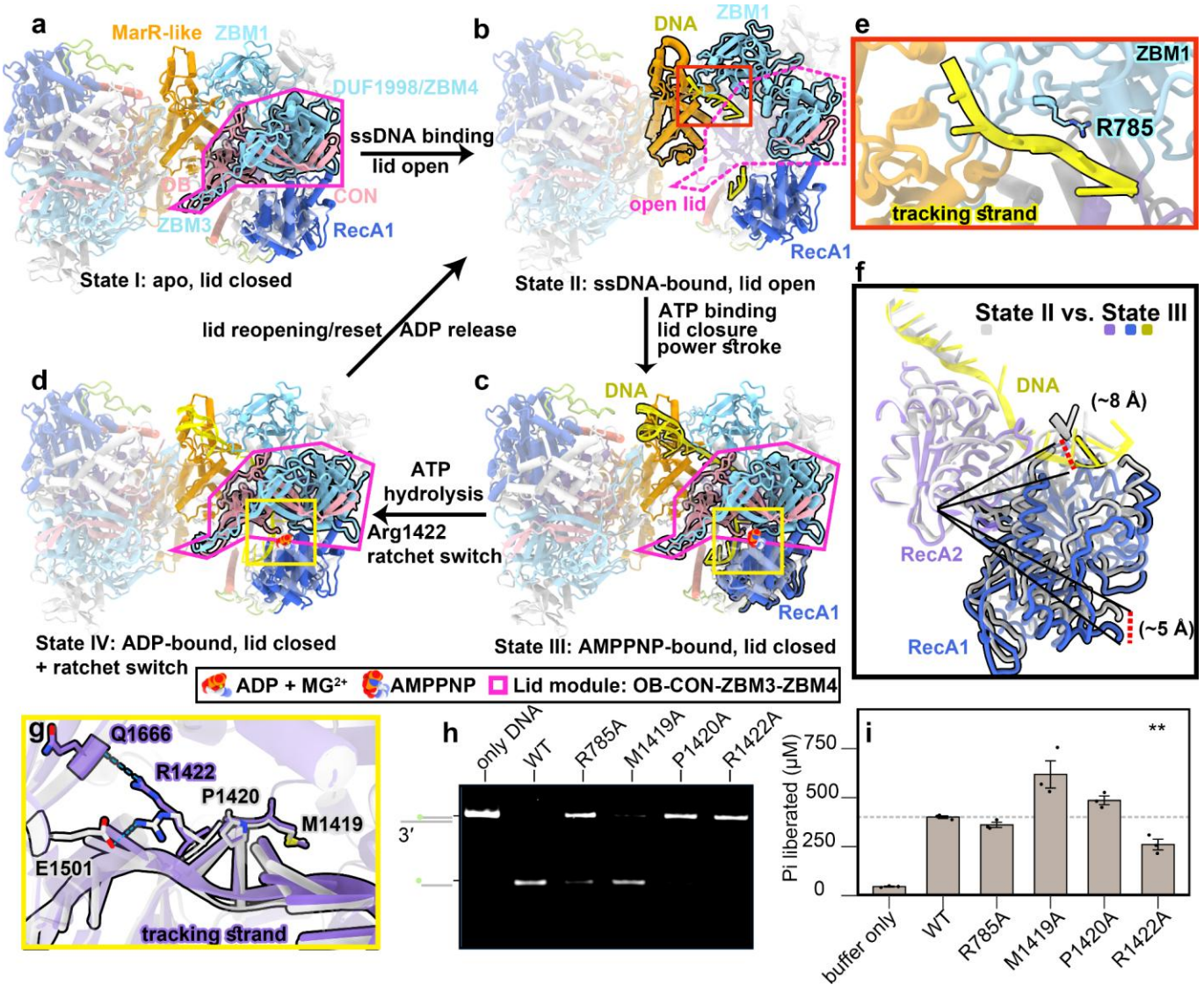

Figure 5. Conformational transitions and biochemical validation of DruE-mediated DNA translocation. (a–d) Structural snapshots of the motor-protomer cycle. State I represents the apo resting state with the lid module ordered over the central channel (a). Upon ssDNA binding, the lid opens and the tracking strand is accommodated in the motor channel in State II (b). AMPPNP binding closes the lid and is associated with a power-stroke-like displacement in State III (c). ATP hydrolysis to the ADP-bound state is accompanied by an R1422-associated ratchet switch in State IV (d). The lid module, comprising the OB, CON, ZBM3 and DUF1998/ZBM4 regions, is outlined in magenta. (e) Enlarged view of the orange boxed region in panel b, shown in the same colour scheme, highlighting R785 in ZBM1 contacting the 3′ tracking strand. (f) Local structural comparison of States II and III, showing movement of the RecA1/RecA2 motor domains and displacement of the DNA. (g) Enlarged comparison of the yellow boxed regions in panels c and d, shown in the same colour scheme, showing nucleotide-state-dependent remodelling of the R1422-containing loop between States III and IV. (h) Native PAGE-based helicase assays comparing WT DruE with alanine-substitution mutants in residues implicated in substrate gating and translocation. (i) DNA-stimulated ATPase activities of WT DruE and the indicated mutants. Data in i are from three independent experiments; statistical significance relative to WT was assessed using two-tailed unpaired Student's t-tests. Statistical significance is indicated as **P < 0.01. See Supplementary Movie 2 for an animation of the motor-protomer cycle.

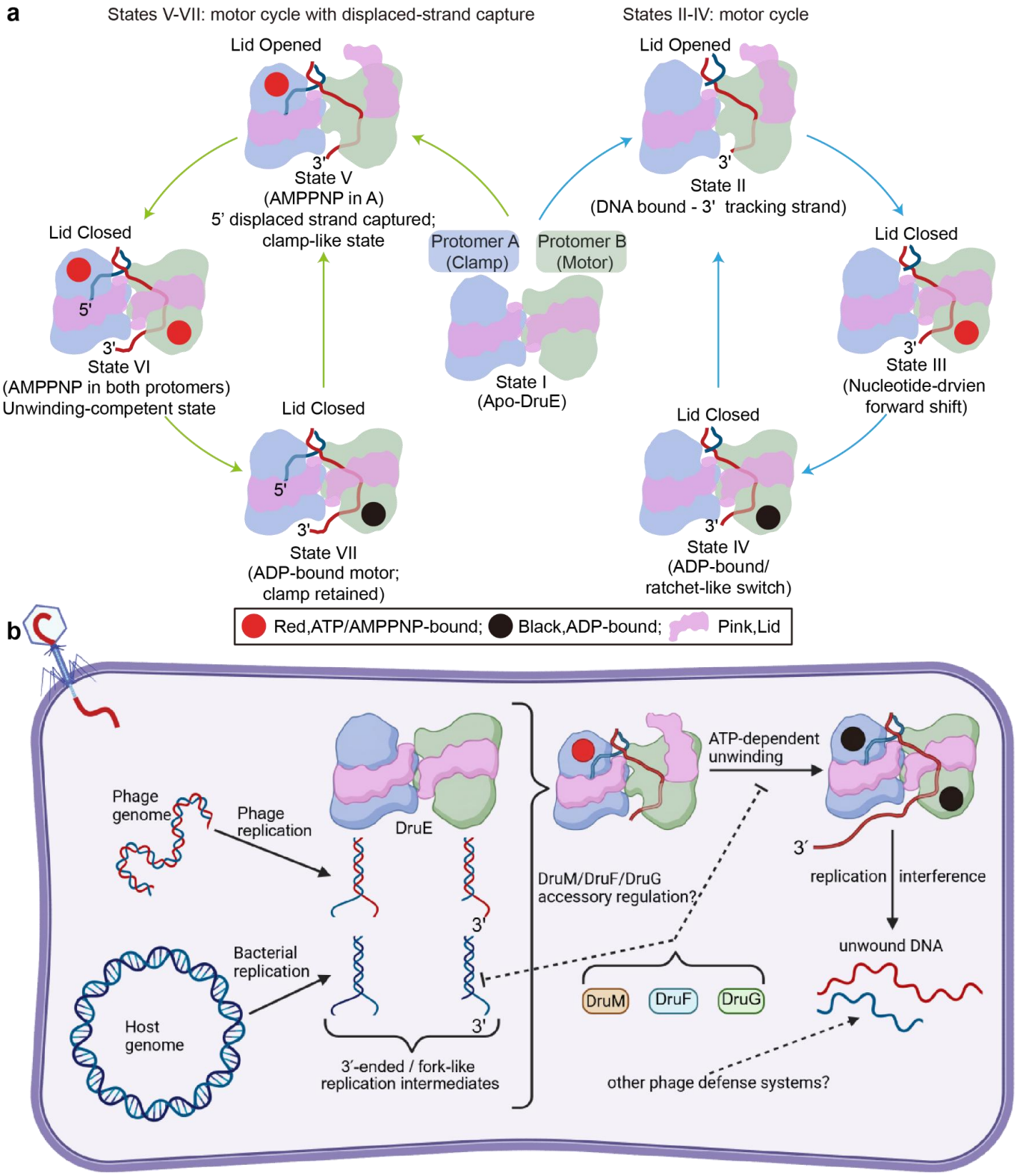

Figure 6. Mechanism of DruE-mediated DNA unwinding and working model for type II Druantia defence. (a) Proposed mechanochemical cycle of the asymmetric DruE homodimer. Protomer B functions as the motor protomer, whereas protomer A functions as the clamp protomer. In States I–IV, DruE undergoes a motor-protomer cycle in which the 3′ tracking strand is loaded into protomer B and nucleotide-dependent lid opening and closure drive directional translocation. In State I, DruE adopts an apo resting state with the lid module ordered over the central channel. ssDNA loading opens the lid and positions the 3′ tracking strand in the motor channel (State II). AMPPNP binding closes the lid and is associated with a power-stroke-like movement along the tracking strand (State III). ATP hydrolysis to the ADP-bound state triggers an R1422-associated ratchet switch that may bias forward translocation (State IV). In States V–VII, protomer A captures the 5′ displaced strand, stabilizes the adjacent duplex arm and acts as a processivity clamp while protomer B continues its nucleotide-dependent motor cycle. Red and black circles indicate AMPPNP- and ADP-bound states, respectively; the magenta module represents the lid. (b) Working model for type II Druantia-mediated antiphage defence and host-associated regulation. During phage genome replication, 3′-ended or fork-like replication intermediates can be generated and recognized by DruE. DruE-mediated ATP-dependent unwinding of these substrates is proposed to interfere with phage DNA replication, producing unwound DNA products and suppressing infection. Similar 3′-ended or fork-like intermediates may also arise during bacterial DNA replication, highlighting the need to constrain DruE activity to avoid host self-damage. Genetic analyses under MMC-induced DNA damage suggest that DruM, DruF and DruG help maintain host fitness and may regulate DruE-associated activity, although direct

regulation has not been experimentally established and is therefore indicated by a dashed arrow. The possibility that DruE-generated unwound DNA engages other phage defence systems is also hypothetical and is shown with a dashed arrow. Solid arrows indicate steps supported by the biochemical and structural data presented here.

References

1. Hampton, H. G., Watson, B. N. J. & Fineran, P. C. The arms race between bacteria and their phage foes. Nature 577, 327–336 (2020).

2. Roberts, R. J. et al. A nomenclature for restriction enzymes, DNA methyltransferases, homing endonucleases and their genes. Nucleic Acids Res 31, 1805–1812 (2003).

3. Makarova, K. S. et al. Evolutionary classification of CRISPR-Cas systems: a burst of class 2 and derived variants. Nat Rev Microbiol 18, 67–83 (2020).

4. Tesson, F. et al. Systematic and quantitative view of the antiviral arsenal of prokaryotes. Nat Commun 13, 2561 (2022).

5. Cohen, D. et al. Cyclic GMP-AMP signalling protects bacteria against viral infection. Nature 574, 691–695 (2019).

6. Millman, A. et al. Bacterial Retrons Function In Anti-Phage Defense. Cell 183, 1551–1561.e12 (2020).

7. Song, X.-Y. et al. Bacterial reverse transcriptase synthesizes long poly(A)-rich cDNA for antiphage defense. Science 388, eads4639 (2025).

8. Antine, S. P. et al. Structural basis of Gabija anti-phage defence and viral immune evasion. Nature 625, 360–365 (2024).

9. Doron, S. et al. Systematic discovery of antiphage defense systems in the

782 microbial pangenome. Science 359, (2018).

783 10. Duncan-Lowey, B. et al. Cryo-EM structure of the RADAR supramolecular anti-
784 phage defense complex. Cell 186, 987–998.e15 (2023).

785 11. Lopatina, A., Tal, N. & Sorek, R. Abortive Infection: Bacterial Suicide as an Antiviral
786 Immune Strategy. Annu Rev Virol 7, 371–384 (2020).

787 12. Fairman-Williams, M. E., Guenther, U.-P. & Jankowsky, E. SF1 and SF2 helicases:
788 family matters. Curr Opin Struct Biol 20, 313–324 (2010).

789 13. O'Leary, N. A. et al. Reference sequence (RefSeq) database at NCBI: current
790 status, taxonomic expansion, and functional annotation. Nucleic Acids Res 44, D733–45
791 (2016).

792 14. Tuck, O. T. et al. Genome integrity sensing by the broad-spectrum Hachiman
793 antiphage defense complex. Cell 187, 6914–6928.e20 (2024).

794 15. Ofir, G. et al. DISARM is a widespread bacterial defence system with broad anti-
795 phage activities. Nat Microbiol 3, 90–98 (2018).

796 16. Bravo, J. P. K., Aparicio-Maldonado, C., Nobrega, F. L., Brouns, S. J. J. & Taylor,
797 D. W. Structural basis for broad anti-phage immunity by DISARM. Nat Commun 13, 2987
798 (2022).

799 17. Payne, L. J. et al. Identification and classification of antiviral defence systems in
800 bacteria and archaea with PADLOC reveals new system types. Nucleic Acids Res 49,
801 10868–10878 (2021).

802 18. Bell, R. T. et al. YprA-family helicases provide the missing link between diverse
803 prokaryotic immune systems. Cell Host Microbe (2026) doi:10.1016/j.chom.2026.05.015.

804 19. Li, Y. & He, Z.-G. Type III Druantia two-component antiphage defense depends on

805 the DruH-DruE interaction for inhibiting viral DNA circularization and replication. Cell
806 Insight 5, 100341 (2026).
807 20. Tomasz, M. Mitomycin C: small, fast and deadly (but very selective). Chem Biol 2,
808 575–579 (1995).
809 21. Räschle, M. et al. Mechanism of replication-coupled DNA interstrand crosslink
810 repair. Cell 134, 969–980 (2008).
811 22. Roske, J. J., Liu, S., Loll, B., Neu, U. & Wahl, M. C. A skipping rope translocation
812 mechanism in a widespread family of DNA repair helicases. Nucleic Acids Res 49, 504–
813 518 (2021).
814 23. Büttner, K., Nehring, S. & Hopfner, K.-P. Structural basis for DNA duplex
815 separation by a superfamily-2 helicase. Nat Struct Mol Biol 14, 647–652 (2007).
816 24. Dumont, S. et al. RNA translocation and unwinding mechanism of HCV NS3
817 helicase and its coordination by ATP. Nature 439, 105–108 (2006).
818 25. Velankar, S. S., Soultanas, P., Dillingham, M. S., Subramanya, H. S. & Wigley, D.
819 B. Crystal structures of complexes of PcrA DNA helicase with a DNA substrate indicate
820 an inchworm mechanism. Cell 97, 75–84 (1999).
821 26. Stelter, M., Acajjaoui, S., McSweeney, S. & Timmins, J. Structural and mechanistic
822 insight into DNA unwinding by Deinococcus radiodurans UvrD. PLoS One 8, e77364
823 (2013).
824 27. Hu, H. et al. Molecular basis of the Druantia anti-phage defense system. bioRxiv
825 2026.05.12.722862 (2026) doi:10.64898/2026.05.12.722862.
826 28. Himpich, S. et al. A compact Druantia defense clears phage infections via single-
827 stranded DNA recognition and directional duplex unwinding. bioRxiv 2026.05.13.724758

(2026) doi:10.64898/2026.05.13.724758.

29. Li, H. et al. The co-localizing Zorya II, Druantia III, and ARMADA II defense systems on O-island 172 confer synergistic anti-phage defense in enterohemorrhagic. mBio e0094326 (2026) doi:10.1128/mbio.00943-26.

30. Wu, Y. et al. Antiphage defence systems Druantia III and Zorya II synergise via shared DNA intermediates in a phage-specific manner. bioRxiv 2026.05.12.724681 (2026) doi:10.64898/2026.05.12.724681.

31. Weigel, C. & Seitz, H. Bacteriophage replication modules. FEMS Microbiol. Rev. 30, 321–381 (2006).

32. Wu, R. & Kaiser, A. D. Structure and base sequence in the cohesive ends of bacteriophage lambda DNA. J Mol Biol 35, 523–537 (1968).

33. Wang, P. et al. Development of an efficient conjugation-based genetic manipulation system for Pseudoalteromonas. Microb. Cell Fact. 14, 11 (2015).

34. Tesson, F. et al. Exploring the diversity of anti-defense systems across prokaryotes, phages and mobile genetic elements. Nucleic Acids Res 53, (2025).

35. Zulkower, V. & Rosser, S. DNA Features Viewer: a sequence annotation formatting and plotting library for Python. Bioinformatics 36, 4350–4352 (2020).

36. Gibson, D. G. et al. Enzymatic assembly of DNA molecules up to several hundred kilobases. Nat Methods 6, 343–345 (2009).

37. Engler, C., Kandzia, R. & Marillonnet, S. A one pot, one step, precision cloning method with high throughput capability. PLoS One 3, e3647 (2008).

38. Punjani, A., Rubinstein, J. L., Fleet, D. J. & Brubaker, M. A. cryoSPARC: algorithms for rapid unsupervised cryo-EM structure determination. Nat Methods 14, 290–296 (2017).

851 39. Cao, H. et al. EMReady2: improvement of cryo-EM and cryo-ET maps by local
852 quality-aware deep learning with Mamba. Nat Commun (2026) doi:10.1038/s41467-026-
853 71794-1.
854 40. Jumper, J. et al. Highly accurate protein structure prediction with AlphaFold.
855 Nature 596, 583–589 (2021).
856 41. Pettersen, E. F. et al. UCSF ChimeraX: Structure visualization for researchers,
857 educators, and developers. Protein Sci 30, 70–82 (2021).
858 42. Emsley, P., Lohkamp, B., Scott, W. G. & Cowtan, K. Features and development of
859 Coot. Acta Crystallogr D Biol Crystallogr 66, 486–501 (2010).
860 43. Croll, T. I. ISOLDE: a physically realistic environment for model building into low-
861 resolution electron-density maps. Acta Crystallogr D Struct Biol 74, 519–530 (2018).
862 44. Liebschner, D. et al. Macromolecular structure determination using X-rays,
863 neutrons and electrons: recent developments in Phenix. Acta Crystallogr D Struct Biol 75,
864 861–877 (2019).
865 45. Chen, V. B. et al. MolProbity: all-atom structure validation for macromolecular
866 crystallography. Acta Crystallogr D Biol Crystallogr 66, 12–21 (2010).
867 46. Dillingham, M. S. & Kowalczykowski, S. C. RecBCD enzyme and the repair of
868 double-stranded DNA breaks. Microbiol Mol Biol Rev 72, 642–71, Table of Contents
869 (2008).
870 47. Domgaard, H. et al. CasDinG is a 5’-3' dsDNA and RNA/DNA helicase with three
871 accessory domains essential for type IV CRISPR immunity. Nucleic Acids Res. 51, 8115–
872 8132 (2023).

873